Through-grid wicking enables high-speed cryoEM specimen preparation

Yong Zi Tan[1] and John L. Rubinstein[1,2,3,*]

[1.] Molecular Medicine Program, The Hospital for Sick Children, Toronto, Ontario, Canada
[2.] Department of Biochemistry, The University of Toronto, Ontario, Canada
[3.] Department of Medical Biophysics, The University of Toronto, Ontario, Canada
* Correspondence: john.rubinstein@utoronto.ca

Abstract

Blotting times for conventional cryoEM specimen preparation complicate time-resolved studies and lead to some specimens adopting preferred orientations or denaturing at the air-water interface. We show that solution sprayed onto one side of a holey cryoEM grid can be wicked through the grid by a glass fiber filter held against the opposite side, often called the 'back' of the grid, producing a film suitable for vitrification. This process can be completed in tens of milliseconds. We combined ultrasonic specimen application and through-grid wicking in a high-speed specimen preparation device that we name 'Back-it-up', or BIU. The high liquid-absorption capacity of the glass fiber compared to self-wicking grids appears to make the method relatively insensitive to the amount of sample applied. Consequently, through-grid wicking produces large areas of ice suitable for cryoEM for both soluble and detergent-solubilized protein complexes. The device's speed increases the number of views for a specimen that suffers from preferred orientations.

Introduction

Advances in single particle electron cryomicroscopy (cryoEM) now allow routine high-resolution structure determination for many macromolecules and molecular assemblies. Nonetheless, the ability to prepare specimens suitable for imaging remains one of the main bottlenecks for these structural studies. Standard specimen preparation methods (Dubochet et al., 1988; Knapek and Dubochet, 1980) involve using a micropipette or syringe to transfer microliter volumes of solution onto the surface of an EM grid coated with a holey carbon or gold film (Figure 1*A*). Excess sample is removed by blotting with paper for seconds to produce a thin aqueous film, which is subsequently vitrified by plunging the grid into a cryogen such as liquid ethane or a mixture of liquid ethane and liquid propane. The liquid-absorption capacity of the paper is far larger than the amount of sample applied, suggesting that blotting for too long should lead to complete drying of the grid. However, once formed, these thin films of solution appear to be moderately stable, with continued blotting only slowly thinning the film (Armstrong et al., 2020). This continued thinning could occur either through further wicking or through evaporation.

Blotting with paper can be done from one or both sides of the grid. If blotting is performed from only one side, it is usually done on the side where the sample was applied. 'Backside blotting', where sample is applied on one side and blotting is performed on the other, has been used to concentrate filaments or particles that cannot pass through the grid holes (Amos and Hirose, 2007). Blotting a 3 μL sample into a 1000 Å thick film that covers a 3 mm diameter EM grid requires removal of 99.998% of the liquid. Consequently, blotting to remove sample without concentrating the molecule of interest on the grid is extraordinarily wasteful. The time required to prepare a thin film by blotting, which is likely due to the large volume of liquid that must be removed, prevents or complicates using grid freezing to study time dependent processes that occur on timescales shorter than a few seconds. During grid preparation, the sample exists as a thin liquid film with a large surface area to volume ratio, exposing fragile macromolecules to nearby hydrophobic air-water interfaces for an extended period. The interaction of protein particles with an air-water interface has been found to induce preferred orientations for many specimens (Noble et al., 2018) and cause denaturation of others (D'Imprima et al., 2019; Glaeser et al., 2016).

55

56 The introduction of self-wicking grids (Razinkov et al., 2016; Wei et al., 2018) provided a new
57 way of preparing cryoEM specimens (Figure 1*B*). With these specimen supports, copper
58 hydroxide nanowires are grown from the copper surface of copper-rhodium grid bars by
59 incubating the grids in a solution of ammonium persulfate at basic pH. The grids are
60 subsequently covered with a sacrificial film of holey plastic (Marr et al., 2014; Razinkov et al.,
61 2016; Wei et al., 2018) that can be coated with carbon or gold before the plastic is dissolved.
62 During specimen freezing, small volumes of liquid are applied onto the nanowire side of the
63 grid. When the liquid contacts the nanowires, most of the sample is wicked to the grid bars,
64 leaving a thin film suitable for vitrification and subsequent imaging. The volume of liquid
65 applied is small and the wicking process occurs quickly, producing a suitable film in tens of
66 milliseconds. However, the nanowires on the grid have a limited capacity to absorb liquid and
67 can be easily saturated if too much sample is applied. Further, the speed of wicking from copper
68 hydroxide-nanowire grids can vary from grid to grid, a problem thought to be due to variability
69 in the copper used to make the grids (Wei et al., 2018). The small droplets of liquid needed for
70 this approach have been generated previously by two different methods, although presumably
71 other liquid dispensing techniques could also be used. In the first application of self-wicking
72 grids, a piezoelectric transducer coupled to a glass capillary, similar to the printing head in an
73 inkjet printer, was used to apply sample (Dandey et al., 2018; Jain et al., 2012). This device,
74 named "Spotiton", led to the commercial "Chameleon" instrument from SPT Labtech Ltd
75 (Darrow et al., 2019). With Spotiton and Chameleon, the sample is applied onto a strip of grid
76 squares as the grid is moved past the dispensing head, allowing the wicking behavior of the grid
77 to be characterized with high-speed cameras. Suitable conditions are selected and the sample is
78 applied to a different strip of grid squares on the same grid before plunge-freezing in cryogen.
79 This approach requires high-precision liquid dispensing and high-quality optical components.
80 Alternatively, liquid can be dispensed in a less controlled manner by a simple piezoelectric
81 transducer like the ones found in ultrasonic humidifiers, an approach implemented with the open-
82 source "Shake-it-off" (SIO) device (Rubinstein et al., 2019). This device relies on the
83 piezoelectric transducer producing a distribution of droplets that varies in intensity across the
84 grid so that some regions are saturated with liquid, some are dry, and some receive an optimal
85 volume to produce ice of an appropriate thickness for imaging.

A drawback of the Shake-it-off device is that it tends to produce only small areas of usable ice, with significant variation from grid to grid. Therefore, we sought to develop a robust approach for cryoEM grid preparation with the speed of self-wicking grids, but with the simplicity of conventional grid preparation. We reasoned that the large excess of absorption capacity during conventional grid preparation allows the process to reach the metastable state of a thin film regardless of the exact volume of sample applied to the grid. We hypothesized that if liquid could wick through a grid, a large absorption capacity available on one side of a holey grid would allow specimens to be prepared by high-speed application of small volumes of liquid to the other side (Figure 1*C*). The large absorption capacity would make the technique insensitive to the precise volume of liquid applied, enabling large areas of specimen to be prepared for cryoEM with a simple, robust, and inexpensive droplet generator. We found that this effect could be achieved by treating both surfaces of the grid with extensive glow discharge in air to make them hydrophilic and using glass fiber to wick excess solution through the grid. Following the naming pattern of the Spotiton and Shake-it-off devices, and recognizing the similarity to the backside blotting approach, we name the device presented here *"*Back-it-up*"* or BIU.

Results and Discussion

Through-grid wicking with glass fiber allows preparation of thin vitreous ice

We investigated the capability of different blotting materials to rapidly wick liquid through a holey grid when applied to the opposite side of the grid. We found that this effect could be achieved consistently with glass fiber filters but not with conventional filter paper. Glass fiber filters have been used previously to prepare cryoEM specimens from carbon nanotubes in chlorosulfonic acid (Talmon, 2015). Scanning electron microscopy (SEM) with secondary electron detection illustrates the relatively large cellulose fibers in conventional filter paper (Figure 2*A*i) compared to the smaller glass fibers (Figure 2*A*ii). Conventional cryoEM grids with a holey gold film on the rhodium surface of copper-rhodium grids were made hydrophilic by extensive glow discharge in air on both sides and laid with their flat gold surface in contact with either conventional filter paper or a glass fiber filter. A high-speed video of water being applied to the copper surface of the grids shows that the liquid is rapidly wicked through the grid by

116 glass fiber, while this phenomenon did not occur consistently with conventional filter paper (Fig
117 2*B*; Movie 1).
118
119 To test if through-grid wicking with glass fiber allows production of thin films of vitreous ice
120 suitable for cryoEM, a specimen of commercially available recombinant hemagglutinin trimer
121 from influenza A virus (Strain A/Hong Kong/1/1968[H3N2]) was prepared with a Gatan
122 Cryoplunge 3 (CP3) grid freezing device. After application of sample to the copper surface of the
123 grid, one sided blotting was performed on the gold surface, with the usual 20 mm circle of filter
124 paper replaced with a 20 mm circle of glass fiber filter. The majority of the 3 µL sample
125 appeared to wick through the grid in ~1 sec and blotting was continued for a total of 5 sec. A
126 cryoEM atlas of the grid showed a gradient of ice thicknesses (Figure 2*C*i), with many grid
127 squares having ice suitable for data collection (Figure 2*C*ii). High magnification images (Figure
128 2*C*iii) of holes with appropriate ice for data collection revealed high-contrast particles similar to
129 micrographs obtained previously with the same hemagglutinin specimen (Tan et al., 2017).
130
131 *Construction of BIU, a high-speed through-grid wicking specimen preparation device*
132 To develop a device that dispenses small volumes of sample for high-speed cryoEM specimen
133 preparation using the through-grid wicking approach, we adapted the open source Shake-it-off
134 platform (Rubinstein et al., 2019) (Figure 1*C*, 3*A*). In the new instrument design (Figure 3),
135 Dumont L5 tweezers holding an EM grid are attached with a magnetic connector to a large
136 solenoid capable of plunging the grid into a cryogen bath. The cryogen bath, which is insulated
137 by a Styrofoam box, is milled from aluminum and uses liquid nitrogen to maintain a ~60:40
138 mixture of propane:ethane in a liquid state (Tivol et al., 2008). The ~30 mm travel distance of the
139 plunging solenoid when energized is reduced to ~16 mm by a 3D-printed plastic ring and a
140 magnetic catch keeps the solenoid in its extended position after it is de-energized. A new plastic
141 process mount was designed and 3D-printed to orient the components necessary for through-grid
142 wicking (Figure 3*B*). On one side of the grid, a wicking assembly (Figure 3*C*) uses a tack and a
143 magnet to hold a 20 mm diameter circle of glass fiber filter that is supported by a thin flexible
144 circle of cellulose acetate. This wicking assembly is attached to a small solenoid on the plastic
145 mount so that in its energized position the glass fiber filter is held flush against the grid (Figure
146 3*D*i). On the other side of the grid the plastic mount holds a 16 mm diameter piezoelectric

147 transducer from an ultrasonic humidifier (Figure 3*E*). The piezoelectric transducer produces a
148 spray of small droplets when a high-frequency signal is applied by the humidifier circuit. A
149 magnet embedded in the Styrofoam insulating box of the cryogen container is held against a reed
150 switch when the box is properly positioned, serving as a safety interlock to prevent premature
151 plunging of the tweezers. The system electronics are controlled, via a custom printed circuit
152 board identical to the one use with the Shake-it-off device, by a Raspberry Pi single board
153 computer running a graphical user interface (GUI) written in *Python3*.
154
155 During specimen preparation, a small volume of sample, such as a few hundred nL to 1 μL, is
156 applied to the surface of the piezoelectric transducer opposite the grid. Energizing the high-
157 frequency generating circuit causes a spray of droplets through the piezoelectric transducer onto
158 the copper surface of the grid. After spreading on the grid, liquid is wicked through the grid by
159 the glass fiber filter. Once spraying is complete, the glass fiber filter is held against the grid for
160 an additional wicking time (e.g. 10 msec), after which the glass fiber filter and acetate are pulled
161 back from the grid by de-energizing the small solenoid (Figure 3*D*ii). The large solenoid is then
162 energized and the grid is plunged into the liquid cryogen. At present, this process is carried out at
163 ambient temperature and humidity. However, we see no reason why the BIU device could not be
164 built in a humidity- and temperature-controlled environment, or any number of other controlled
165 environments for specific experiments. Because there is no splash shield for the cryogen, eye
166 protection must always be worn when operating the device. The piezoelectric transducer
167 produces an aerosol from the sample and consequently the device should not be used to prepare
168 samples where aerosols present a health hazard, such as infectious virus particles, some toxins,
169 and infectious prions. However, the device can be installed in a biosafety cabinet to overcome
170 this limitation.
171
172 *High-resolution 3D reconstruction from a specimen prepared with the* BIU *device*
173 In order to determine if the BIU device is able to prepare specimens amenable to high-resolution
174 cryoEM, we used it to prepare multiple grids with human light chain apoferritin. Spraying was
175 done with the piezoelectric transducer energized for 100 msec, with an additional 100 msec
176 delay after spraying and before plunging. This spraying time is twenty times longer than was
177 used with the Shake-it-off device with self-wicking grids and is sufficient to completely saturate

178 copper-hydroxide nanowire grids, leading to thick ice (Rubinstein et al., 2019). CryoEM atlases
179 of the resulting specimen grids show a gradient of ice thicknesses (Figure 4*A*, *upper*). This
180 gradient could be due to spatial variation in the amount or droplet size of the spray from the
181 piezoelectric transducer on different parts of the grid. Alternatively, it could be due to the
182 gradient of pressure with which the glass fiber filter is pressed against the grid, with less pressure
183 near the edge of the glass fiber filter circle and more pressure where the glass fiber filter is
184 secured to the wicking assembly by the tack. Nonetheless, grids consistently had approximately
185 one third of their surface covered with ice suitable for imaging. Apoferritin particles can be seen
186 clearly in high-magnification images from multiple grids (Figure 4*A*, *lower*), demonstrating that
187 the device reproducibly produces specimens with large areas of thin vitreous ice suitable for data
188 collection. A dataset of 3,168 movies was collected from two of the grids (Table 1), allowing
189 calculation of a 3D map at 2.0 Å from 594,259 single particle images (Figure 4*B* and *C,* Figure
190 S1*A* and *B*). An atomic model was built into the density map, including water molecules that
191 could be resolved clearly (Figure 4*C*), confirming that the BIU device is capable of preparing
192 samples that can be used for high-resolution structure determination.
193
194 *The* BIU *device can prepare samples of detergent-solubilized membrane proteins*
195 Membrane proteins maintained in solution with detergents present a unique challenge for
196 cryoEM grid preparation as the detergents often lead to specimens with a steep gradient of ice
197 thickness (Rubinstein, 2007). In order to determine if the BIU device and the through-grid
198 wicking approach can prepare high-quality cryoEM specimens when detergents are present in
199 samples, we vitrified cryoEM grids of two different membrane proteins samples that included *n*-
200 dodecyl β-D-maltoside (DDM). These samples were a yeast ATP synthase (Guo et al., 2017)
201 (Figure 5*A*) and a bacterial ATP synthase complex (Figure 5*B*). Similar to the apoferritin grids,
202 large areas of usable ice were produced for these specimens. High-magnification images from
203 thin vitreous ice show the membrane protein complexes clearly. These particle images allowed
204 calculation of 2D class average images with high-resolution features, confirming that the BIU
205 device can be used with detergent-containing membrane protein samples.
206

207 *High-speed through-grid wicking can reduce time-dependent preferred orientations*
208 With the Spotiton device and self-wicking grids, the influenza A hemagglutinin trimer was
209 shown to undergo time-dependent adoption of a preferred top-view orientation at the air-water
210 interface during grid freezing (Noble et al., 2018). This preferred orientation can prevent
211 calculation of a 3D map. In that study, conventional use of a Gatan CP3 (~1 sec blot time)
212 resulted in most particles adopting the three-fold symmetric top views and only 4% of particle
213 images assigned to classes that show a side view of the trimer. In contrast, the number of particle
214 images contributing to side view classes increased to 9% with the Spotiton device and a 500
215 msec spot-to-plunge time, and to 19% with a 100 msec spot-to-plunge time (Noble et al., 2018).
216
217 To determine if specimen preparation with through-grid wicking can be performed at sufficient
218 speed to reduce adoption of preferred orientations, grids were prepared with the BIU device
219 using the identical recombinant hemagglutinin trimer. Sample was sprayed onto the grid with the
220 piezoelectric transducer energized for 30 msec, with an additional 30 msec delay after spraying
221 and before plunging to allow wicking of excess solution by the glass fiber filter. Recording this
222 process at 480 fps (frames per second) showed that the piezoelectric circuit was active for ~45
223 msec, followed by an additional ~30 msec where the grid remained in contact with the glass fiber
224 filter, and ~60 msec passing during which the glass fiber filter was fully retracted and the grid
225 plunged into cryogen (Figure 6*A*, Movie 2). This sequence constitutes an overall process time of
226 135 msec, with immersion in cryogen occurring 90 msec after the end of spraying and 60 msec
227 after breaking contact between the grid and glass fiber filter. 1,556 movies were acquired from
228 this specimen. As with the apoferritin and ATP synthase specimens, approximately one third of
229 the grid had ice that was suitable for imaging. 1,284 movies were also acquired from a sample of
230 the hemagglutinin trimer, described earlier, that was prepared using the Gatan CP3 with glass
231 fiber filter paper and backside blotting. With the Gatan CP3 and a 5 sec blot time, 2% of particle
232 images (1,506 out of 91,879) were assigned to a single class corresponding to a side view, while
233 98% (90,373 out of 91,879) were assigned to classes that showed top views or oblique views
234 (Figure 6*B*). In contrast, with the BIU grid 66% of particle images (170,419 out of 256,303) were
235 assigned to top or oblique view classes while 34% (85,884 out of 256,303) were assigned to side-
236 view classes (Figure 6*B*). The top and oblique views for the BIU specimen also appeared to
237 include more tilted oblique views than for the Gatan CP3 specimen (Figure 6*B*, *left*). The large

238 number of single particle images presenting side views in the BIU specimen allowed 3D
239 reconstruction of the hemagglutinin trimer at 2.9 Å resolution (Figure 6*C*, Figure S2*A* and *B*,
240 Table 1) without the need for tilting the specimen (Tan et al., 2017). The high quality of the map
241 allowed construction of an atomic model, including three N-linked glycans (Figure 6*D, bottom*
242 *right*). The map has a sampling compensation factor (Baldwin and Lyumkis, 2020) of 0.92 and a
243 3D Fourier shell correlation sphericity (Tan et al., 2017) of nearly 1.00 when calculated either
244 between half-maps or between the map and the model (Figure 6*C*, Figure S2*B*, Table 1). These
245 statistics support the directional isotropy of the resolution. Local resolution in the map is slightly
246 worse near the membrane proximal part of the trimer (Figure 6*C, bottom of map*) as was
247 suggested previously for this complex (Vilas et al., 2020), likely due flexibility in the structure.
248
249 **Discussion**
250 Implementation of through-grid wicking for high-speed cryoEM specimen preparation allows
251 grids to be frozen in tens of milliseconds, rather than the multiple seconds needed for
252 conventional grid preparation. The method does not require the self-wicking nanowire grids used
253 previously in the Spotiton, Chameleon, and Shake-it-off devices. Avoiding nanowire grids and
254 using conventional holey cryoEM grids simplifies the consumables needed for grid preparation
255 and reduces a source of variability that has affected specimen preparation with nanowire grids
256 (Wei et al., 2018). By providing a high capacity for absorbing liquid, through-grid wicking
257 appears to increase the tolerance for excess-liquid applied to the grid. This decrease in sensitivity
258 avoids creation of large areas of ice that are too thick for data collection, even when
259 approximately six to twenty times the spraying time of the Shake-it-off device (Rubinstein et al.,
260 2019) is used with the BIU device, or 3 µL of sample is applied directly to the grid in the Gatan
261 CP3. As a result, large areas of high-quality ice can be prepared readily and reproducibly with
262 the BIU device, with approximately one third of the grid surface available for data collection.
263 This large usable area allows for straightforward structure determination from a single grid.
264
265 Electron tomography of specimens prepared with the Spotiton device showed that the
266 mechanism for reducing preferred orientations was decreased interaction with the thin film air-
267 water interface before freezing (Noble et al., 2018). Although repeating the mechanistic analysis
268 of this effect with the BIU device is beyond the scope of the present manuscript, which instead

269 focuses on the ability of the approach to prepare usable specimens, the abundance of
270 hemagglutinin trimer side views is presumably due to the same effect that occurs when
271 performing high-speed grid preparation with self-wicking grids.
272
273 In the experiments described above we used the same ultrasonic specimen application approach
274 employed with the Shake-it-off instrument, which is related to an acoustic wave atomization
275 approach described previously (Ashtiani et al., 2018). However, through-grid wicking can almost
276 certainly be used with other methods for applying sample onto an EM grid. The piezoelectric
277 transducer from an ultrasonic humidifier used here has the advantage of having no 'dead volume'
278 of sample that must be loaded into the device but cannot be dispensed. It has the disadvantage of
279 using relatively large volumes for each grid, such as hundreds of nanoliters up to one microliter,
280 although it may be possible to reduce this volume further. Alternative sample application
281 methods include the ink-jet approach implemented in the Spotiton device (Dandey et al., 2018;
282 Jain et al., 2012) and the microfluidic sprayers used with several time-resolved specimen
283 preparation devices (Feng et al., 2017; Kaledhonkar et al., 2018; Kontziampasis et al., 2019; Lu
284 et al., 2014). Through-grid wicking could also prove useful for preparing optimal ice when
285 applying nanoliter samples to a grid with a microcapillary (Arnold et al., 2017, 2016) or from a
286 solid surface (Ravelli et al., 2020).
287
288 Similar to the Shake-it-off platform on which it is based, the BIU instrument is inexpensive to
289 construct. The implementation described here cost ~C$1,000 (~USD$700) to build, or
290 approximately 500 to 1000× less than a commercially available second-generation grid
291 preparation device. All components needed to build the device are either commercially available
292 or can be made by online 3D printing, printed circuit board fabrication, and CNC milling
293 services, so that specialized manufacturing infrastructure is not required. The 3D design files, the
294 printed circuit board design files, and the control software are available online to allow others to
295 easily replicate the instrument (https://github.com/johnrubinstein). We believe that the
296 reproducibility and large areas of usable ice from through-grid wicking, combined with the
297 simplicity and low construction cost of the BIU device, provides a robust and easily accessible
298 approach to high-speed cryoEM grid preparation for a variety of specimens.

Author contributions

JLR devised the grid preparation approach, built the instrument, and wrote the control software. YZT devised the characterization strategy, prepared samples, collected data, performed image analysis, and constructed atomic models. JLR and YZT wrote the manuscript and prepared the figures

Acknowledgements

Recombinant human apoferritin was a gift from Taylor Sicard and Jean-Philippe Julien (The Hospital for Sick Children). Recombinant yeast ATP synthase was prepared by Hui Guo (The Hospital for Sick Children). Recombinant bacterial ATP synthase was prepared by Gautier Courbon (The Hospital for Sick Children). We thank Ali Darbandi (The Hospital for Sick Children) for performing the SEM imaging in Figure 2. We thank Drs. Glaeser and Han (Lawrence Berkeley National Laboratory) for confirming that the through-grid wicking phenomenon is not due to surfactant on the glass fiber filter. YZT was supported by a postdoctoral fellowship from the Canadian Institutes of Health Research and JLR was supported by the Canada Research Chairs program. This work was supported by a Discovery Grant from the Natural Sciences and Engineering Research Council. CryoEM data was collected at the Toronto High-Resolution High-Throughput cryoEM facility, supported by the Canada Foundation for Innovation and Ontario Research Fund.

Declaration of interests

YZT and JLR have filed a patent application related to the specimen preparation approach described in this manuscript.

Data availability

All raw movies, micrographs, particle stacks, and relevant metadata files will be deposited into EMPIAR. CryoEM maps of apoferritin and hemagglutinin have been deposited into the EMDB as EMD- 21951 and EMD-21954 respectively. Models of apoferritin and hemagglutinin have been deposited into the PDB as 6WX6 and 6WXB. Original software and 3D design files are available from https://github.com/johnrubinstein

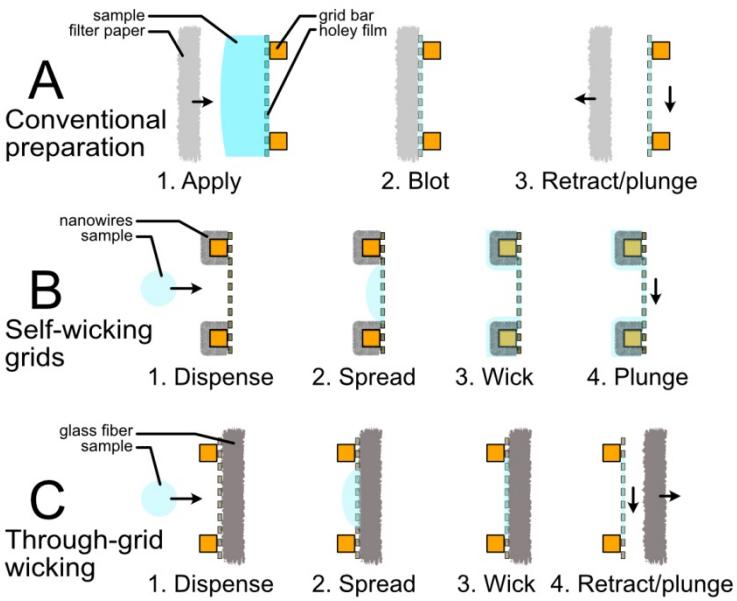

Figure 1. Cartoon of different wicking approaches for cryoEM specimen preparation approaches. (*A***)** Conventional specimen preparation: the sample is applied to the grid and blotted with filter paper to produce a thin film suitable for plunge freezing. (*B*) Self-wicking grids: nanowires on the grid absorb excess liquid to produce a thin film. Small volumes of the sample are applied by a piezoelectric inkjet dispenser (Spotiton) or piezoelectric transducer (Shake-it-off). (*C*) Through-grid wicking: the sample is applied to one side of the grid while a filter on the other side removes excess sample to produce the film that will be vitrified.

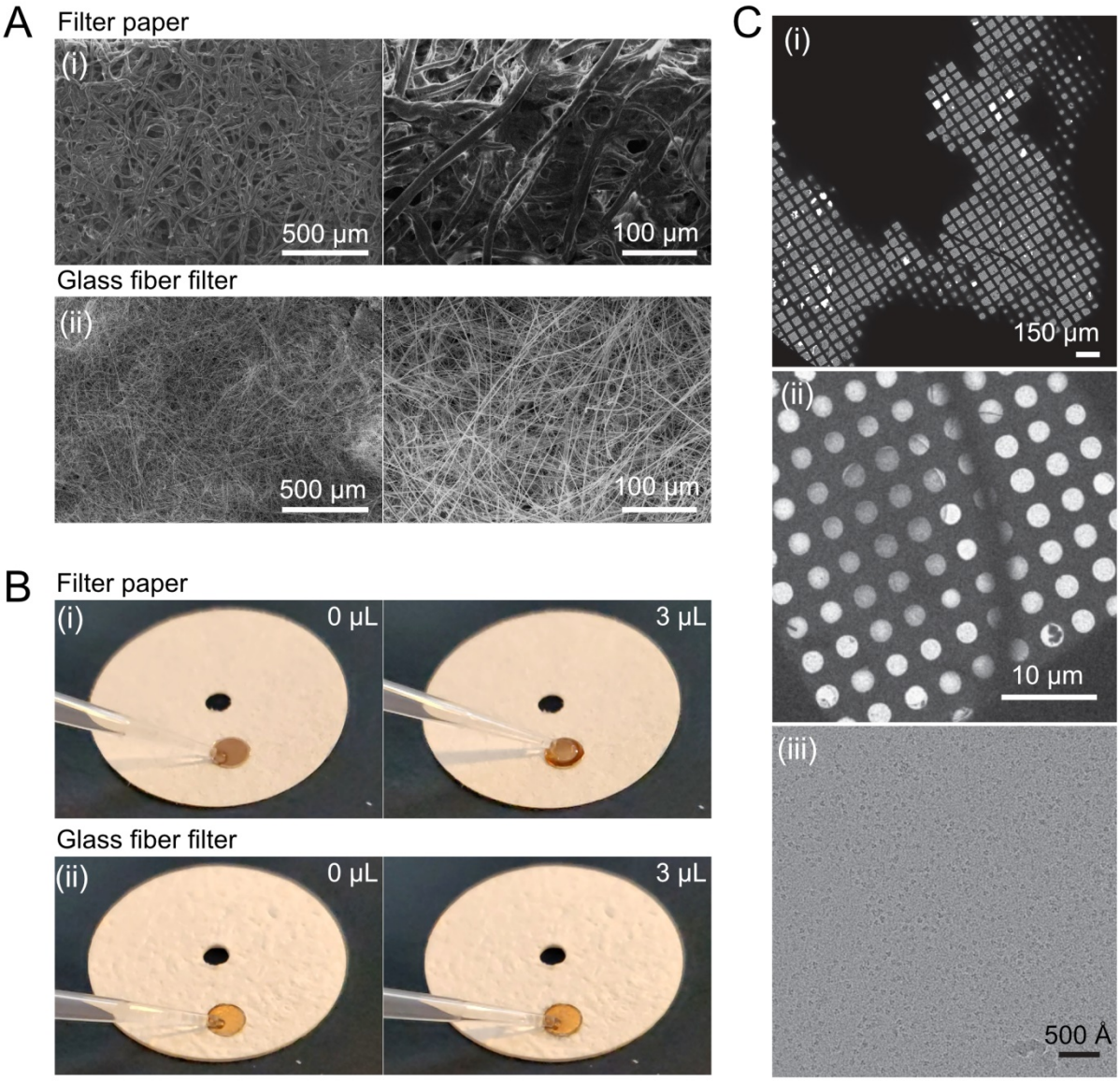

Figure 2. Through-grid wicking with glass fiber. (*A*) Scanning electron microscopy (SEM) images of conventional filter paper (i) and glass fiber filter (ii) at two magnifications. (*B*) A holey gold grid previously subjected to glow discharged on both sides does not consistently show rapid through-grid wicking when in contact with filter paper (i) but water quickly wicks through the grid when it is placed on a glass fiber filter (ii). Movie 1 shows this process in more detail. (*C*) A hemagglutinin trimer specimen prepared by through-grid wicking with a Gatan CP3 grid freezing device and glass fiber filter. A grid atlas (i), grid square (ii), and high magnification image (iii) are shown.

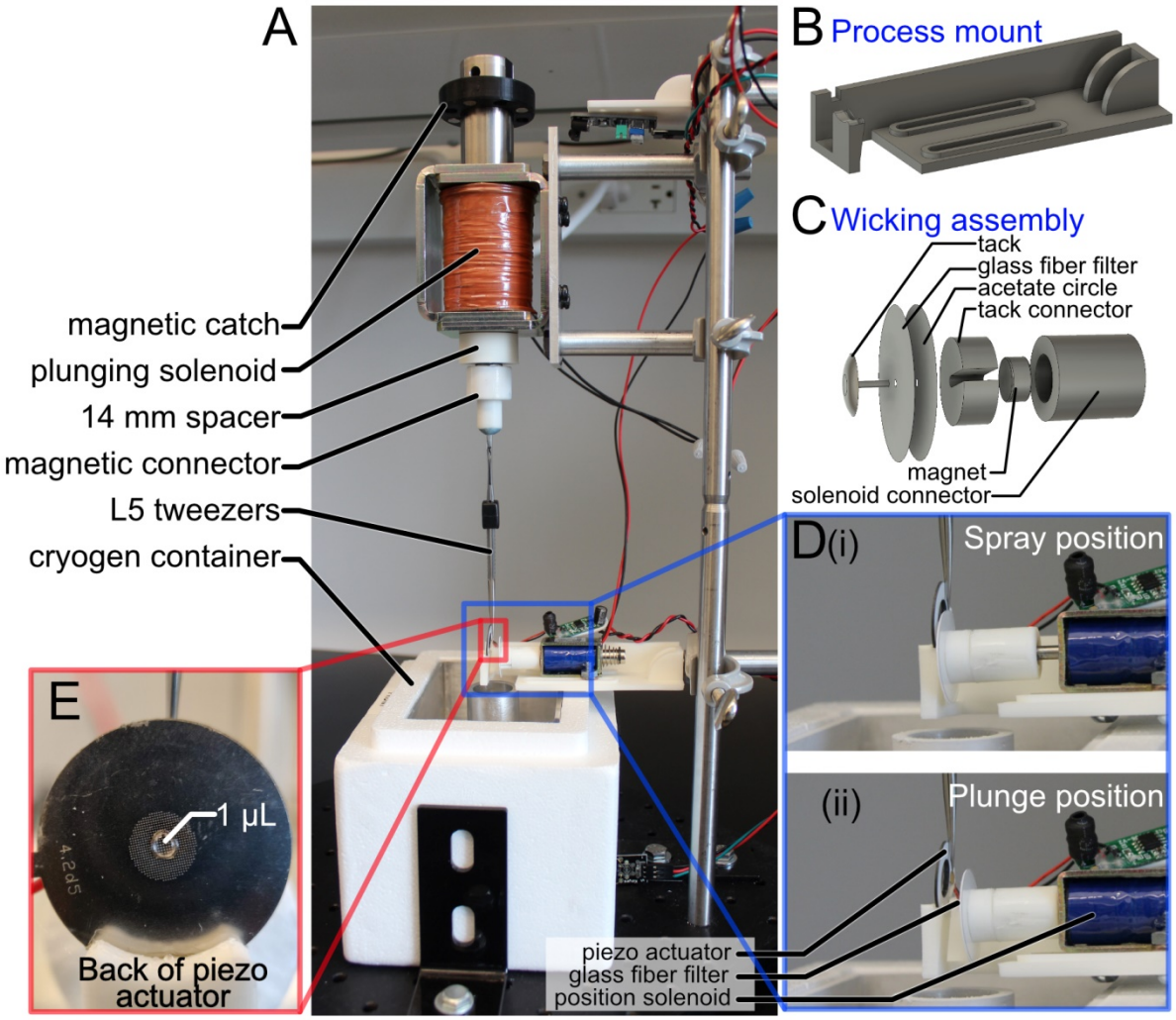

Figure 3. The Back-it-up (BIU) device. (*A*) Fully assembled BIU specimen-preparation device. In comparison with the SIO device, new components are the process mount (*B*) and wicking assembly (*C*). (*D*) When the position solenoid is energized the wicking assembly holds the glass fiber filter flush against the grid to allow spraying and through-grid wicking (i). When the position solenoid is de-energized, the glass fiber filter is retracted creating the clearance needed to plunge the grid into cryogen (ii). (*E*) Sample is applied to the back of the piezoelectric transducer before spraying.

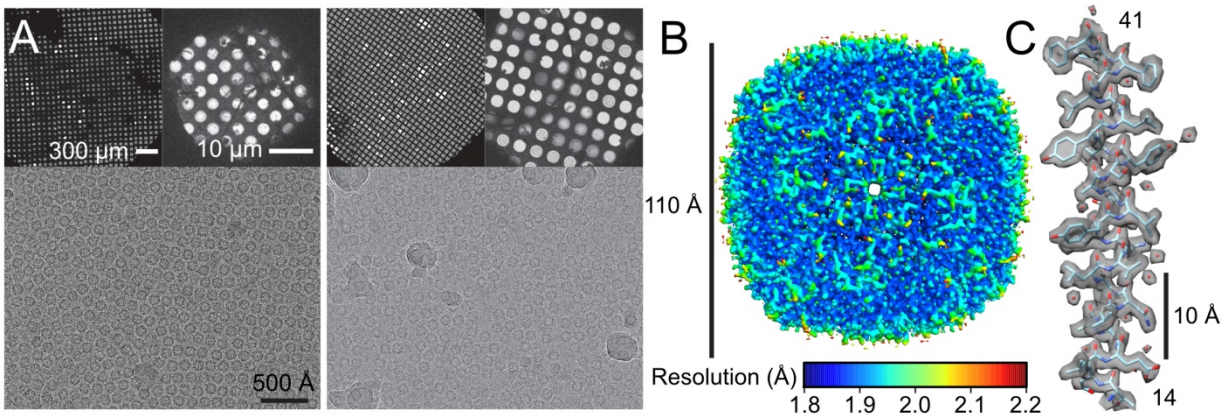

Figure 4. Human apoferritin vitrified using BIU. (*A*) Grid atlases, grid squares, and micrographs from human apoferritin prepared for cryoEM using BIU. (*B*) Local resolution for the apoferritin reconstruction. (*C*) A representative α helix from the apoferritin model (residues 14 to 41) and the experimental density map (grey surface). Water molecules are displayed as red spheres.

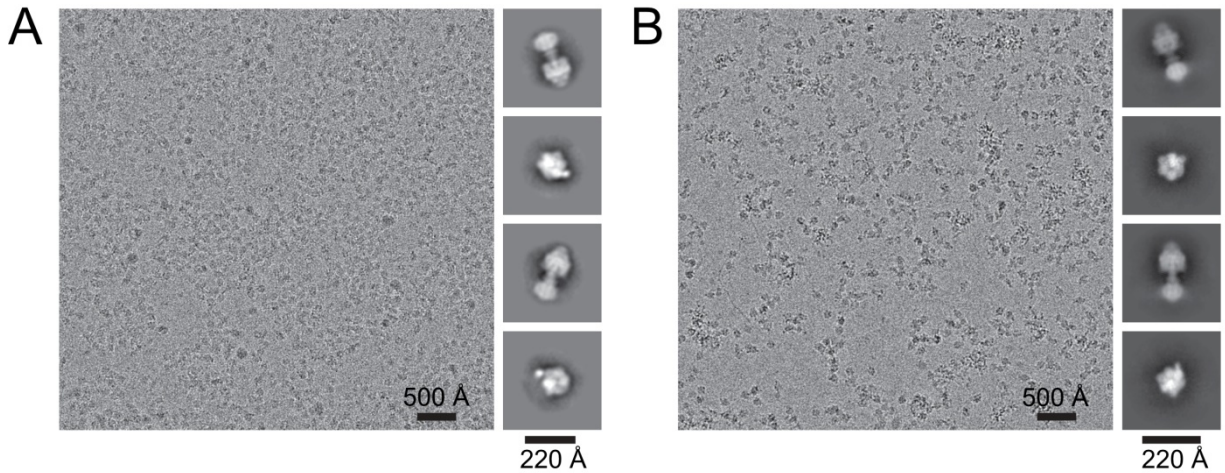

371
372
373 **Figure 5. Membrane proteins solubilized in detergent vitrified using BIU.** (*A*) Representative
374 high-magnification image of yeast ATP synthase and r2D class averages. (*B*) Representative
375 high-magnification image of bacterial ATP synthase complex and representative 2D class
376 averages.
377

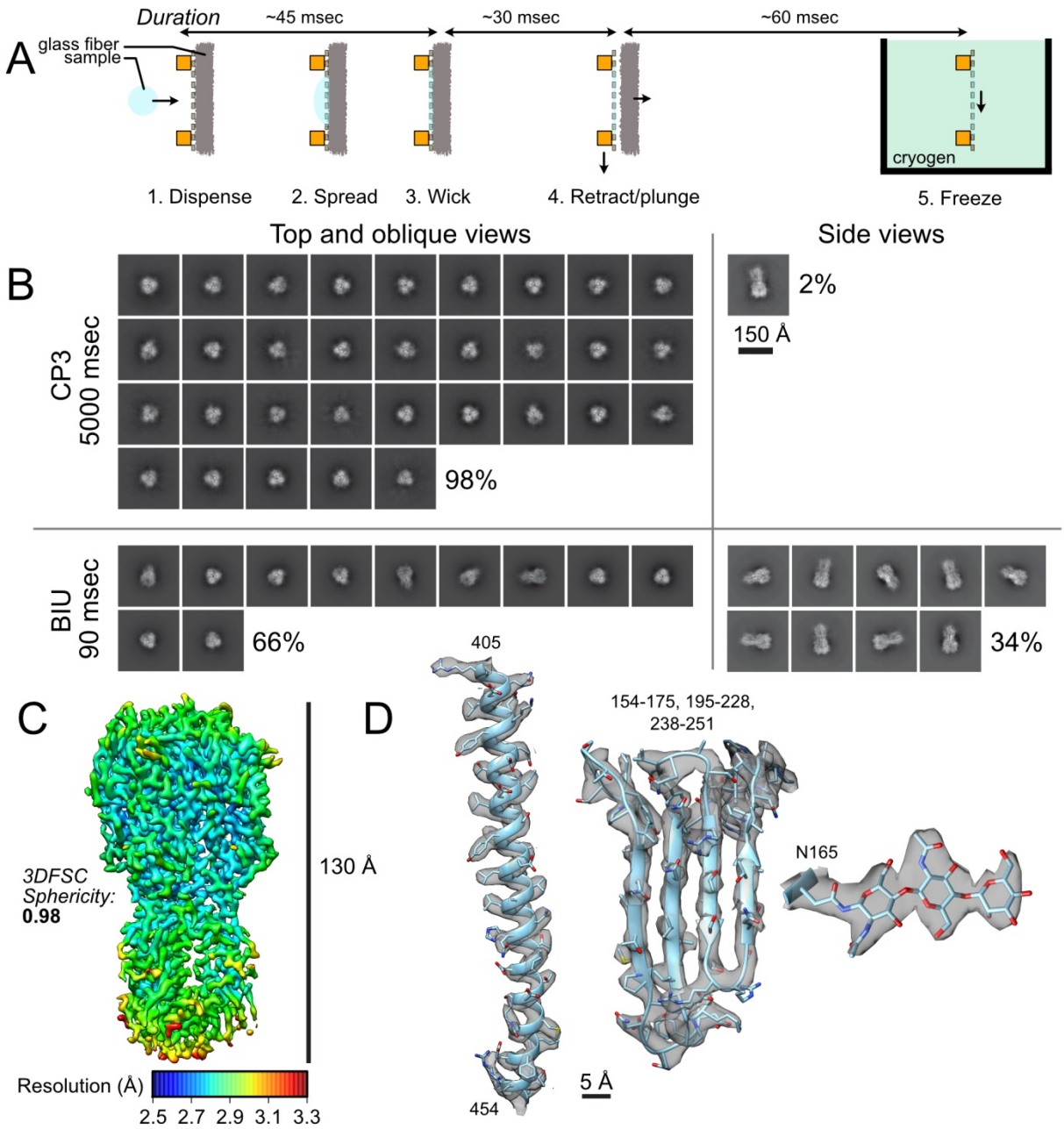

Figure 6. High-speed freezing with BIU improves the orientation distribution in a hemagglutinin trimer specimen. (*A*) Timing of the grid freezing process measured with high-speed video. (*B*) The complete set of 2D class averages from hemagglutinin trimer specimens prepared with the Gatan CP3 and BIU. The fraction of particle images contributing to top and oblique view classes versus side view classes is indicated. (*C*) Local resolution map of the hemagglutinin trimer. (*D*) A representative α helix (residues 405-454), β sheet (residues 154-175, 195-228, 238-251), and N-glycan (residue 165) from the hemagglutinin model, overlaid with the experimental density map (grey surface).

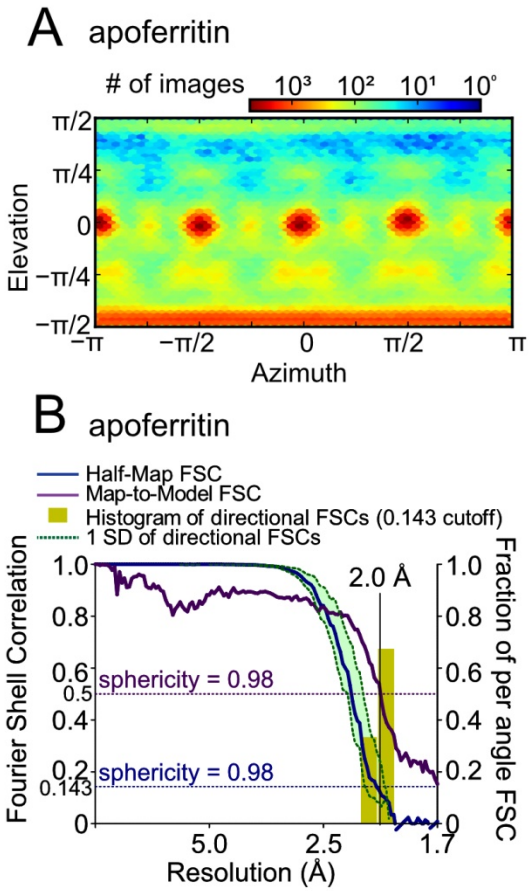

Figure S1. CryoEM map validation. (*A*) Euler angle distribution for human light chain apoferritin. *(B)* Fourier shell correlation (FSC) curves for human light chain apoferritin show the map resolution from half-map (blue) and map-to-model (purple) correlation at FSC=0.143 and FSC=0.5, respectively. A histogram of directional resolutions sampled evenly over the 3DFSC (yellow) is also shown and the corresponding sphericity is indicated.

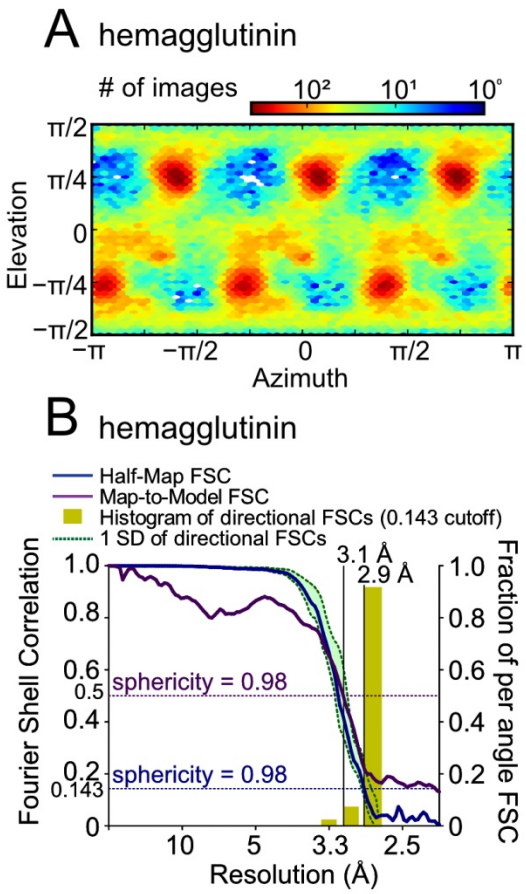

Figure S2. CryoEM map validation. (*A*) Euler angle distribution for influenza A H3N2 hemagglutinin trimer. *(B)* Fourier shell correlation (FSC) curves for influenza A H3N2 hemagglutinin trimer show the map resolution from half-map (blue) and map-to-model (purple) correlation at FSC=0.143 and FSC=0.5, respectively. A histogram of directional resolutions sampled evenly over the 3DFSC (yellow) is also shown and the corresponding sphericity is indicated.

Movie 1. Comparison of filter paper and glass fiber filter for through-grid wicking. Water (5 μL) applied to a hydrophilic holey gold grid does not consistently wick through the grid when it is placed on filter paper (top) but quickly wicks through the grid when it is placed on a glass fiber filter (bottom).

Movie 2. High speed video of the BIU process. A video recorded at 480 frames per second shows the high-frequency generating circuit of the piezoelectric transducer energized for ~45 msec. A further 30 msec elapses where the glass fiber filter remains in contact with the grid. The grid is plunged into cryogen ~60 msec after it breaks contact with the glass fiber filter.

415 **Table 1. Cryo-EM data collection and modeling statistics**

	Human L Chain Apoferritin (BIU)	Hemagglutinin (CP3)	Hemagglutinin (BIU)
EM data collection / processing			
Microscope	FEI Titan Krios		
Voltage (kV)	300		
Camera	Falcon 4		
Mode	Counting		
Defocus mean ± std (μm)	0.7 ± 0.4	2.0 ± 0.5	2.0 ± 0.5
Exposure time (s)	9	9	9
Number of fractions	29	29	29
Exposure rate (e^-/pixel/s)	3	5	5
Total exposure ($e^-/Å^2$)	40	40	40
Pixel size (Å)	0.816	1.03	1.03
Number of micrographs	3,168	1,284	1,556
Number of particles (after cleanup)	673,794	232,841	378,143
Number of particles (in final map)	594,259	-	128,305
Symmetry	O	-	C3
Resolution (global) (Å)	2.0	-	2.9
Local Resolution Range	1.8-2.2	-	2.5-3.4
Directional Resolution Range	1.9-2.1	-	2.7-3.2
Sphericity of 3DFSC	0.98	-	0.98
SCF Value*	1.00	-	0.92
Map B factor ($Å^2$)	92.8	-	150.9
Model statistics			
Residue range	5-176	-	9-325, 334-501
Map CC	0.88	-	0.77
RMSD [bonds] (Å)	0.006	-	0.011
RMSD [angles] (Å)	1.003	-	1.194
All-atom clashscore	0.14	-	2.45
Average B factors ($Å^2$)		-	
Protein	14.91	-	72.39
Ligands	23.45	-	69.53
Water	16.18	-	-
Ramachandran plot		-	
Favored (%)	98.82	-	93.56
Allowed (%)	1.18	-	6.03
Outliers (%)	0.00	-	0.42
Rotamer outliers	0.00	-	0.94
C-β deviations	0.00	-	0.00
MolProbity Score	0.53	-	1.45
EM-Ringer Score	7.70	-	4.07

416 *The sampling compensation factor (SCF) value is calculated as described (Baldwin and Lyumkis, 2020) and
417 assumes that all orientations have been determined accurately.

418 **Materials and Methods**
419 *Device design, construction, and consumables*
420 New 3D parts were designed with *Autodesk Fusion 360* and printed in polylactic acid with a
421 Raise3D Pro2 3D printer. All other parts and components were identical to those used with the
422 SIO device (Rubinstein et al., 2019). 20 mm circles of glass fiber filters (VWR grade 691) and
423 filter paper (Whatman #1) were cut with the circle punch from the Gatan CP3 grid freezing
424 device. Nanofabricated holey gold film coated EM grids with regularly spaced ~2 µm holes were
425 prepared on EMS Maxtaform 400 mesh Cu/Rh grids as described previously (Marr et al., 2014).
426 Grids were glow discharged in air for two minutes on each side with a PELCO easiGlow (Ted
427 Pella) immediately before use.
428
429 *Apoferritin specimen preparation*
430 Human apoferritin light chain (UniProtKB: P02792), modified with an N-terminal Strep tag and
431 linker, a C-terminal extension, and a K173R mutation, was a gift from Taylor Siccard and Jean-
432 Philippe Julien (The Hospital for Sick Children). Apoferritin was diluted to 5 to 10 mg/mL for
433 specimen preparation with BIU. Sample (1 µL) was applied to the piezoelectric transducer and
434 liquid was transferred to the grid by energizing the high-frequency generating circuit for 100
435 msec. An additional 100 msec was allowed for the glass fiber filter to wick sample through the
436 grid before retracting the filter and plunging the grid into the liquid propane/ethane bath.
437
438 *Yeast ATP synthase specimen preparation*
439 Yeast ATP synthase was a gift from Hui Guo. Yeast ATP synthase was diluted to 10 mg/mL
440 with 0.05% (w/v) DDM for specimen preparation with BIU. Sample (1 µL) was applied to the
441 piezoelectric transducer and liquid was transferred to the grid by energizing the high-frequency
442 generating circuit for 50 msec. An additional 1000 msec was allowed for the glass fiber filter to
443 wick sample through the grid before retracting the filter and plunging the grid into the liquid
444 propane/ethane bath.
445
446 *Bacterial ATP synthase specimen preparation*
447 Bacterial ATP synthase was a gift from Gautier Courbon. The protein was diluted to 2 mg/mL
448 with 0.05% (w/v) DDM for specimen preparation with BIU. Sample (1 µL) was applied to the
449 piezoelectric transducer and liquid was transferred to the grid by energizing the high-frequency
450 generating circuit for 10 msec. An additional 500 msec was allowed for the glass fiber filter to
451 wick sample through the grid before retracting the filter and plunging the grid into the liquid
452 propane/ethane bath.
453
454 *Hemagglutinin specimen preparation*
455 Hemagglutinin (MyBioSource product MBS434205) was used without dilution (1 mg/mL). For
456 specimen preparation with the Gatan Cryoplunge 3, sample (3 µL) was applied onto the copper
457 side of nanofabricated gold grids in the environmental chamber of the device (>80% RH, 298 K).
458 Grids were blotted from only the gold side of the grid with glass fiber filter for 5 sec and plunged
459 into liquid ethane. For freezing hemagglutinin with the BIU device, sample (1 µL) was applied to
460 the piezoelectric transducer and liquid was transferred to the grid by energizing the high-
461 frequency generating circuit for 30 msec. An additional 30 msec was allowed for the glass fiber
462 filter to wick sample through the grid before retracting the filter and plunging the grid into the

liquid propane/ethane bath. High-speed movies were recorded at 480 frames per second with a rolling shutter using a OnePlus6 mobile phone.

CryoEM data collection

ATP synthase data was acquired at 200 kV with a FEI Tecnai F20 electron microscope and Gatan K2 summit camera operating in electron counting mode. Data collection was done manually using Digital Micrograph software. 50 movies were collected for the yeast ATP synthase, and 107 movies were collected for the bacterial ATP synthase at a pixel size of 1.45 Å/pixel. Movies were collected for 15 sec with 30 exposure fractions, a camera exposure rate of ~8 e^-/pix/sec, and total specimen exposure of ~50 $e^-/Å^2$.

For apoferritin and hemagglutinin, data was acquired at 300 kV with a Thermo Fisher Scientific Titan Krios G3 electron microscope and prototype Falcon 4 camera operating in electron counting mode at 250 frames/sec. The microscope was automated with the *EPU* software package and data collection was monitored with *cryoSPARC Live* (Punjani et al., 2017).

3,168 movies were acquired from two grids of apoferritin prepared with BIU. The pixel size was calibrated at 0.816 Å/pixel by fitting a crystal structure of human ferritin L chain (PDB ID: 2FFX) (Wang et al., 2006) into a preliminary 3D map. Movies were collected for 9 sec with 29 exposure fractions, a camera exposure rate of ~3 e^-/pix/sec, and total specimen exposure of ~40 $e^-/Å^2$. A 100 µm objective aperture was used. 1,284 movies were acquired from one grid with hemagglutinin prepared with the CP3. The pixel size was calibrated at 1.03 Å/pixel from a gold diffraction standard. Movies were collected for 9 sec with 29 exposure fractions, a camera exposure rate of ~5 e^-/pix/sec, and a total specimen exposure of ~40 $e^-/Å^2$. No objective aperture was used. 1,556 movies were acquired from one grid with hemagglutinin prepared with the BIU device. The calibrated pixel size was 1.03 Å. Movies were collected for 9 sec with 29 exposure fractions, a camera exposure rate of ~5 e^-/pix/sec, and a total specimen exposure of ~40 $e^-/Å^2$. No objective aperture was used.

Apoferritin image processing

Exposure fractions were aligned with *MotionCor2* (Zheng et al., 2017) within *Relion* (Kimanius et al., 2016; Scheres, 2012), using 7×7 patches and a B factor of 500 $pixel^2$ for global alignment and 150 $pixel^2$ for local alignment. Micrographs were then imported into *cryoSPARC* (Punjani et al., 2017) and patch CTF estimation was performed. Templates generated from 2D classification during the *cryoSPARC Live* session were used for template selection of particles. 2D classification was used to remove junk particles, resulting in a dataset of 673,794 particle images. An additional round of 2D and 3D classification reduced the dataset to 594,259 particle images. Homogeneous refinement with global and local CTF refinement was then performed and the refined defocus values, Euler angles, and shifts were exported to *Relion*. Particle polishing was done in *Relion* (Zivanov et al., 2019). The particle images were imported back into *cryoSPARC* for a final round of homogeneous refinement with global and local CTF refinement, producing a 2.0 Å map. Octahedral symmetry was enforced throughout all 3D refinement steps. Transfer of data between *Relion* and *cryoSPARC* were done with *pyem* (10.5281/zenodo.3576630).

Hemagglutinin image processing

Movies were aligned with patch motion correction and patch CTF estimation was performed in *cryoSPARC*. Particle images were selected by blob picking with multiple rounds of 2D classification to remove junk particles. This process resulted in 232,841 hemagglutinin particle images for the specimen prepared with the CP3 grid freezing device. The process gave 378,143 hemagglutinin particle images for the specimen prepared with the BIU device. For 3D structure determination, local motion correction was performed on these particles, followed by repeated rounds of *ab initio* 3D classification with two classes to remove junk particles. The final stack of 128,305 particle images was used to produce a map at 2.9 Å resolution by homogeneous refinement with C3 symmetry enforced and CTF refined globally and locally.

Model building and refinement

A crystal structure of human light chain ferritin (PDB ID: 2FFX) (Wang et al., 2006) was used to start model building for apoferritin and a crystal structure of the influenza A H3N2 hemagglutinin (PDB ID: 3WHE) (Iba et al., 2014) was used to start model building for hemagglutinin. Models were built manually in *Coot* (Emsley and Cowtan, 2004) and refined with iterative rounds of adjustment in *Coot* and real space refinement with *Phenix* (Adams et al., 2010; Afonine et al., 2018). This process was continued until statistics calculated with *Molprobity* (Chen et al., 2010) ceased to improve. Restraints for the ligands were generated with *phenix.ready_set*. The calcium ion in the apoferritin structure was identified by comparison with a previous apoferritin structure (PDB ID: 1Z6O) (Hamburger et al., 2005). The final map and model were validated using *EMRinger* (Barad et al., 2015) to compare map to model, *cryoSPARC*'s implementation of *blocres* (Cardone et al., 2013) to assess map local resolution, the *3DFSC* suite (Tan et al., 2017) to calculate directional resolution anisotropy, and the *SCF* program (Baldwin and Lyumkis, 2020) to calculate the sampling compensation factor (SCF), which quantifies how preferred particle orientations contribute to attenuation of the Fourier shell correlation (FSC). Map-to-model FSCs were calculated by converting the model to a map with the *molmap* function in *Chimera* at the Nyquist resolution. A mask was made from this map with *Relion* (after low-pass filtering to 8 Å, extending by 1 pixel, and applying a cosine-edge of 3 pixels), and was applied to the map. Map-to-model FSC was calculated with *proc3d* in *EMAN* (Ludtke et al., 1999).

Bibliography

Adams PD, Afonine P V., Bunkóczi G, Chen VB, Davis IW, Echols N, Headd JJ, Hung LW, Kapral GJ, Grosse-Kunstleve RW, McCoy AJ, Moriarty NW, Oeffner R, Read RJ, Richardson DC, Richardson JS, Terwilliger TC, Zwart PH. 2010. PHENIX: A comprehensive Python-based system for macromolecular structure solution. *Acta Cryst* **D66**:213–221. doi:10.1107/S0907444909052925

Afonine P V., Poon BK, Read RJ, Sobolev O V., Terwilliger TC, Urzhumtsev A, Adamsa PD. 2018. Real-space refinement in PHENIX for cryo-EM and crystallography research papers. *Acta Cryst* **D74**:531–544. doi:10.1107/S2059798318006551

Amos LA, Hirose K. 2007. Studying the Structure of Microtubules by Electron Microscopy. *Methods Mol Med* **137**:65–91.

Armstrong M, Han B, Gomez S, Turner J, Fletcher DA, Glaeser RM. 2020. Microscale Fluid Behavior during Cryo-EM Sample Blotting. *Biophys J* **118**:708–719. doi:10.1016/j.bpj.2019.12.017

Arnold SA, Albiez S, Bieri A, Syntychaki A, Adaixo R, McLeod RA, Goldie KN, Stahlberg H, Braun T. 2017. Blotting-free and lossless cryo-electron microscopy grid preparation from nanoliter-sized protein samples and single-cell extracts. *J Struct Biol* **197**:220–226. doi:10.1016/j.jsb.2016.11.002

Arnold SA, Albiez S, Opara N, Chami M, Schmidli C, Bieri A, Padeste C, Stahlberg H, Braun T. 2016. Total Sample Conditioning and Preparation of Nanoliter Volumes for Electron Microscopy. *ACS Nano* **10**:4981–4988. doi:10.1021/acsnano.6b01328

Ashtiani D, Venugopal H, Belousoff M, Spicer B, Mak J, Neild A, de Marco A. 2018. Delivery of femtolitre droplets using surface acoustic wave based atomisation for cryo-EM grid preparation. *J Struct Biol* **203**:94–101. doi:10.1016/j.jsb.2018.03.012

Baldwin PR, Lyumkis D. 2020. Non-uniformity of projection distributions attenuates resolution in. *Prog Biophys Mol Biol* **150**:160–183. doi:10.1016/j.pbiomolbio.2019.09.002

Barad BA, Echols N, Wang RYR, Cheng Y, Dimaio F, Adams PD, Fraser JS. 2015. EMRinger: Side chain-directed model and map validation for 3D cryo-electron microscopy. *Nat Methods* **12**:943–946. doi:10.1038/nmeth.3541

Cardone G, Heymann JB, Steven AC. 2013. One number does not fit all: Mapping local variations in resolution in cryo-EM reconstructions. *J Struct Biol* **184**:226–236. doi:10.1016/j.jsb.2013.08.002

Chen VB, Arendall WB, Headd JJ, Keedy DA, Immormino RM, Kapral GJ, Murray LW, Richardson JS, Richardson DC. 2010. MolProbity: all-atom structure validation for macromolecular crystallography. *Acta Cryst* **D66**:12–21. doi:10.1107/S0907444909042073

D'Imprima E, Floris D, Joppe M, Sanchez R, Grininger M, Kuhlbrandt W. 2019. Protein denaturation at the air-water interface and how to prevent it. *Elife* **8**:e42747.

Dandey VP, Wei H, Zhang Z, Tan YZ, Acharya P, Eng ET, Rice WJ, Kahn PA, Potter CS, Carragher B. 2018. Spotiton: New features and applications. *J Struct Biol* **202**:161–169. doi:10.1016/j.jsb.2018.01.002

Darrow MC, Moore JP, Walker RJ, Doering K, King RS. 2019. Chameleon : Next Generation Sample Preparation for CryoEM based on Spotiton. *Microsc Microanal* **25**:994–995. doi:10.1017/S1431927619005701

Dubochet J, Adrian M, Chang JJ, Homo JC, Lepault J, McDowall AW, Schultz P. 1988. Cryo-electron microscopy of vitrified specimens. *Q Rev Biophys* **21**:129–228.

Emsley P, Cowtan K. 2004. Coot: Model-building tools for molecular graphics. *Acta Cryst*

585 **D60**:2126–2132. doi:10.1107/S0907444904019158
586 Feng X, Fu Z, Kaledhonkar S, Jia Y, Shah B, Jin A, Liu Z, Sun M, Chen B, Grassucci RA, Ren
587 Y, Jiang H, Frank J, Lin Q. 2017. A Fast and Effective Microfluidic Spraying-Plunging
588 Method for High-Resolution Single-Particle Cryo-EM. *Structure* **25**:663–670.
589 doi:10.1016/j.str.2017.02.005
590 Glaeser RM, Han BG, Csencsits R, Killilea A, Pulk A, Cate JHD. 2016. Factors that Influence
591 the Formation and Stability of Thin, Cryo-EM Specimens. *Biophys J* **110**:749–755.
592 doi:10.1016/j.bpj.2015.07.050
593 Guo R, Zong S, Wu M, Gu J, Yang M. 2017. Architecture of Human Mitochondrial Respiratory
594 Megacomplex I2III2IV2. *Cell* **170**:1247-1257.e12. doi:10.1016/j.cell.2017.07.050
595 Hamburger AE, Jr APW, Hamburger ZA, Hamburger P, Bjorkman PJ. 2005. Crystal Structure of
596 a Secreted Insect Ferritin Reveals a Symmetrical Arrangement of Heavy and Light Chains.
597 *J Mol Biol* **349**:558–569. doi:10.1016/j.jmb.2005.03.074
598 Iba Y, Fujii Y, Ohshima N, Sumida T, Kubota-koketsu R, Ikeda M. 2014. Conserved
599 Neutralizing Epitope at Globular Head of Hemagglutinin in H3N2 Influenza Viruses. *J*
600 *Virol* **88**:7130–7144. doi:10.1128/JVI.00420-14
601 Iudin A, Korir PK, Salavert-Torres J, Kleywegt GJ, Patwardhan A. 2016. EMPIAR: a public
602 archive for raw electron microscopy image data. *Nat Methods* **13**:387–388.
603 Jain T, Sheehan P, Crum J, Carragher B, Potter CS. 2012. Spotiton: A prototype for an integrated
604 inkjet dispense and vitrification system for cryo-TEM. *J Struct Biol* **179**:68–75.
605 doi:10.1016/j.jsb.2012.04.020
606 Kaledhonkar S, Fu Z, White H, Frank J. 2018. Time-Resolved Cryo-electron Microscopy Using
607 a Microfluidic Chip. *Methods Mol Biol* **1764**:59–71. doi:10.1007/978-1-4939-7759-8_4
608 Kimanius D, Forsberg BO, Scheres SHW, Lindahl E. 2016. Accelerated cryo-EM structure
609 determination with parallelisation using GPUs in RELION-2. *Elife* **5**:e18722.
610 doi:10.7554/eLife.18722
611 Knapek E, Dubochet J. 1980. Beam damage to organic material is considerably reduced in cryo-
612 electron microscopy. *J Mol Biol* **141**:147–161. doi:10.1016/0022-2836(80)90382-4
613 Kontziampasis D, Klebl DP, Iadanza MG, Scarff CA, Kopf F, Sobott F, Monteiro DCF, Trebbin
614 M, Muench SP, White HD. 2019. A cryo-EM grid preparation device for time-resolved
615 structural studies. *IUCr J* **6**:1024–1031.
616 Lu Z, Barnard D, Shaikh TR, Meng X. 2014. Gas-assisted annular microsprayer for sample
617 preparation for time-resolved cryo-electron microscopy. *J Micromechanics*
618 *Microengineering* **24**:115001. doi:10.1088/0960-1317/24/11/115001
619 Ludtke SJ, Baldwin PR, Chiu W. 1999. EMAN: semiautomated software for high-resolution
620 single-particle reconstructions. *J Struct Biol* **128**:82–97. doi:10.1006/jsbi.1999.4174S1047-
621 8477(99)94174-6 [pii]
622 Marr CR, Benlekbir S, Rubinstein JL. 2014. Fabrication of carbon films with approximately 500
623 nm holes for cryo-EM with a direct detector device. *J Struct Biol* **185**:42–47.
624 doi:10.1016/j.jsb.2013.11.002
625 Noble AJ, Dandey VP, Wei H, Brasch J, Chase J, Acharya P, Tan YZ, Zhang Z, Kim LY, Scapin
626 G, Rapp M, Eng ET, Rice WJ, Cheng A, Negro CJ, Shapiro L, Kwong PD, Jeruzalmi D,
627 Georges A des, Potter CS, Carragher B. 2018. Routine single particle CryoEM sample and
628 grid characterization by tomography. *Elife* **7**:e34257. doi:10.7554/eLife.34257
629 Punjani A, Rubinstein JL, Fleet DJ, Brubaker MA. 2017. cryoSPARC: Algorithms for rapid
630 unsupervised cryo-EM structure determination. *Nat Methods* **14**:290–296.

doi:10.1038/nmeth.4169
Ravelli RBG, Nijpels FJT, Henderikx RJM, Weissenberger G, Thewessem S, Gijsbers A, Beulen BWAMM, López-Iglesias C, Peters PJ. 2020. Cryo-EM structures from sub-nl volumes using pin-printing and jet vitrification. *Nat Commun* **11**:1–9. doi:10.1038/s41467-020-16392-5
Razinkov I, Dandey VP, Wei H, Zhang Z, Melnekoff D, Rice WJ, Wigge C, Potter CS, Carragher B. 2016. A new method for vitrifying samples for cryoEM. *J Struct Biol* **195**:190–198. doi:10.1016/j.jsb.2016.06.001
Rubinstein JL, Guo H, Ripstein ZA, Haydaroglu A, Au A, Yip CM, Trani JM Di, Benlekbir S, Kwok T. 2019. Shake-it-off: A simple ultrasonic cryo-EM specimen preparation device. *Acta Cryst* **D75**:632125. doi:10.1101/632125
Rubinstein JLL. 2007. Structural analysis of membrane protein complexes by single particle electron microscopy. *Methods* **41**:409–416. doi:S1046-2023(06)00122-8 [pii]10.1016/j.ymeth.2006.07.019
Scheres SHW. 2012. RELION: implementation of a Bayesian approach to cryo-EM structure determination. *J Struct Biol* **180**:519–530. doi:10.1016/j.jsb.2012.09.006
Talmon Y. 2015. The study of nanostructured liquids by cryogenic-temperature electron microscopy - A status report. *J Mol Liq* **210**:2–8. doi:10.1016/j.molliq.2015.03.054
Tan YZ, Baldwin PR, Davis JH, Williamson JR, Potter CS, Carragher B, Lyumkis D. 2017. Addressing preferred specimen orientation in through tilting. *Nat Methods* **14**:793–796. doi:10.1038/nmeth.4347
Tivol WF, Briegel A, Jensen GJ. 2008. An improved cryogen for plunge freezing. *Microsc Microanal* **14**:375–379. doi:10.1017/S1431927608080781
Vilas JL, Tagare HD, Vargas J, Carazo JM, Sorzano COS. 2020. Measuring local-directional resolution and local anisotropy in cryo-EM maps. *Nat Commun* **11**:1–7. doi:10.1038/s41467-019-13742-w
Wang Z, Li C, Ellenburg M, Ruble J, Ho JX, Carter DC. 2006. Structure of human ferritin L chain research papers. *Acta Cryst* **D62**:800–806. doi:10.1107/S0907444906018294
Wei H, Dandey VP, Zhang Z, Raczkowski A, Rice WJ, Carragher B, Potter CS. 2018. Optimizing “self-wicking” nanowire grids. *J Struct Biol* **202**:170–174. doi:10.1016/j.jsb.2018.01.001
Zheng SQ, Palovcak E, Armache J-P, Verba KA, Cheng Y, Agard DA. 2017. MotionCor2 : anisotropic correction of beam-induced motion for improved cryo-electron microscopy. *Nat Methods* **14**:331–332. doi:10.1038/nmeth.4193
Zivanov J, Nakane T, Scheres SHW. 2019. A Bayesian approach to beam-induced motion correction in cryo-EM single-particle analysis. *IUCrJ* **6**:5–17. doi:10.1107/S205225251801463X